Experimental and theoretical modelling of kinetic and equilibrium Ba isotope fractionation during calcite and aragonite precipitation

Vasileios Mavromatis, Kirsten van Zuilen, Marc Blanchard, Mark van Zuilen, Martin Dietzel, Jacques Schott

To cite this version:

Vasileios Mavromatis, Kirsten van Zuilen, Marc Blanchard, Mark van Zuilen, Martin Dietzel, et al.. Experimental and theoretical modelling of kinetic and equilibrium Ba isotope fractionation during calcite and aragonite precipitation. Geochimica et Cosmochimica Acta, 2020, 269, pp.566-580. ⟨10.1016/j.gca.2019.11.007⟩. ⟨hal-02995152⟩

HAL Id: hal-02995152
https://hal.science/hal-02995152v1

Submitted on 9 Nov 2020

Experimental and theoretical modelling of kinetic and equilibrium Ba isotope fractionation during calcite and aragonite precipitation

Vasileios Mavromatis[1,2], Kirsten van Zuilen[3,4], Marc Blanchard[1], Mark van Zuilen[4], Martin Dietzel[2], Jacques Schott[1]

[1] Geosciences Environnement Toulouse (GET), Observatoire Midi-Pyrénées, Université de Toulouse, CNRS, IRD, UPS, 14 Avenue Edouard Belin, 31400 Toulouse, France

[2] Institute of Applied Geosciences, Graz University of Technology, Rechbauerstrasse 12, 8010, Graz, Austria

[3] Department of Earth Sciences, Vrije Universiteit Amsterdam, De Boelelaan 1085, 1081 HV Amsterdam, The Netherlands

[4] Institut de Physique du Globe de Paris, Université Paris Diderot, Université Sorbonne Paris Cité, CNRS UMR 7154, 1 rue Jussieu, 75005, Paris, France

Abstract

Barium isotope fractionation during calcite and aragonite inorganic precipitation was studied in mixed flow reactors as a function of precipitation rate at 25°C and pH = 6.3±0.1. The measured Ba isotope fractionation that occurs between calcite and the forming fluid in the investigated range of calcite growth rates ($10^{-8.0} \leq R_{p(calcite)} \leq 10^{-7.3}$ mol/m^2/s) is insignificant. Barium isotope fractionation between aragonite and the fluid decreases with increasing precipitation rate from $\Delta^{137/134}Ba_{aragonite\text{-}fluid}$ = + 0.25±0.06 ‰ for $R_{p(aragonite)} \leq 10^{-8.7}$ mol/m^2/s to – 0.10±0.08‰ for $R_{p(aragonite)} = 10^{-7.6}$ mol/m^2/s, thus reflecting preferential incorporation of either heavy or light Ba isotopes in aragonite at slow and fast growth rates, respectively. The dependence of Ba isotope fractionation on aragonite growth rate is well described by the surface reaction kinetic model developed by DePaolo (2011) when the values + 0.27 ‰ and - 2.0±0.2‰ are used for the equilibrium and kinetic Ba isotope fractionation factor, respectively. The enrichment of aragonite in the heavier Ba isotopes is consistent with the equilibrium fractionation factor of + 0.34‰, calculated here between Ba-substituted aragonite and Ba^{2+} (aq), from first-principles calculations. This positive fractionation is related to a shorter average Ba-O bond length in the aragonite structure while the coordination number does not change much (i.e. 9). The lack of isotope fractionation between the Ba aquo ions and the 6-coordinated Ba in calcite likely suggests that the coordination reduction required for the incorporation in the lattice of Ba adsorbed at calcite growing sites proceeds without isotope fractionation with the fluid. Otherwise the precipitated calcite should have been enriched in heavy isotopes by ~0.17‰, as predicted by first-principles calculations. These results are the first experimental measurements of Ba isotope fractionation during inorganic calcite and aragonite mineral formation and set the basis for understanding the mechanisms controlling Ba isotope composition in $CaCO_3$ minerals that is an essential perquisite for application of this isotopic system in natural samples.

Keywords: Ba isotope fractionation; calcite; aragonite; growth rate; first-principles calculations

1. Introduction

Several tools used in paleo-environmental reconstruction studies are based on the incorporation of traces / impurities in the crystal lattice of carbonate minerals grown from natural fluids. Among these exchange reactions the most well studied is the replacement of Ca^{2+} in $CaCO_3$ minerals calcite and aragonite by other divalent cations and most commonly the alkaline earth metals Mg^{2+}, Sr^{2+} and Ba^{2+} (Lorens, 1981; Mucci and Morse, 1983; Tesoriero and Pankow,1996; Dietzel et al., 2004; Tang et al., 2008b; Goetschl et al., 2019). The ability over the last two decades to accurately measure the isotopic composition of these elements in natural geomaterials provides now a new set of tools for the exploration of the environmental conditions in the geological past. Among the divalent metals (i.e. Me^{2+}) that have been widely studied are Ca and Mg as they are both highly concentrated in seawater, and also constituting major elements of calcite, Mg-calcites and dolomite. As such, their isotopic variations in natural waters and carbonate samples account for several dozen published studies as shown by the recent reviews of Gussone and Dietzel (2016) and Teng (2017), for Ca and Mg respectively. The isotopic variations of other divalent alkaline earth and transition metals such as Sr^{2+}, Ba^{2+}, Ni^{2+} and Zn^{2+} in natural carbonate archives have also been studied but to a lesser extent, likely because the mechanisms controlling these isotopic variations are not yet thoroughly explored.

Recently the stable isotope composition of barium in minerals including carbonates and sulphates has been proposed as a novel tracer of the barium cycle (Horner et al., 2017; Liu et al., 2019). This is because barium occurs in seawater at trace level concentrations and it obeys a nutrient-like distribution that follows that of dissolved Si and alkalinity (Chow and Goldberg, 1960; Wolgemuth and Broecker, 1970; Jeandel et al., 1996). The barium oceanic chemistry is almost exclusively regulated by the solubility of barite (i.e. $BaSO_4$; Monnin and Galinier, 1988;

Hemsing et al., 2018). Actually recent studies on Ba isotope composition of natural barites provide essential information for the use of this isotopic system as a proxy for Ba input and output in the ocean as well as on the formation conditions of barite (Horner et al., 2015; 2017). Although Ba is incorporated only in trace amounts in $CaCO_3$ minerals calcite and aragonite (Pingitore and Eastman, 1985; Böttcher and Dietzel, 2010), this alkaline earth is a good candidate for a detailed study of its isotopic behaviour during carbonate-fluid interactions because the Ba/Ca ratios of carbonates precipitated from seawater is commonly used as indicator of oceanic circulation and/or freshwater runoff (e.g. Shen and Boyle, 1988; Hall and Chan, 2004; Montaggioni et al., 2006). In order to elucidate however the processes that may affect the Ba isotope composition of natural $CaCO_3$ minerals, experimental studies are necessary. This is because, as it has been observed in other isotopic systems, processes like mineral growth kinetics (Tang et al., 2008a; Boehm et al., 2012), temperature (Li et al., 2012), aqueous complexation (Mavromatis et al., 2019; Füger et al., 2019b) or surface complexation (Füger et al., 2019a) may control the isotopic composition of the solid.

To date Ba isotope measurements in carbonate minerals are relatively scarce. Barium isotope fractionation between solutions and $BaCO_3$ (witherite) and the double carbonate $BaMn[CO_3]_2$ has been investigated experimentally at ambient temperature (von Allmen et al., 2010; Böttcher et al., 2012; 2018a; 2018b; Mavromatis et al., 2016). These studies suggest that the forming carbonates are slightly enriched in the lighter Ba isotope, a feature that is also observed for Ca, Mg and Sr (Tang et al., 2008a; Pearce et al., 2012; Mavromatis et al; 2016; 2017a). The isotopic compositions of Ba in terrestrial carbonates and as trace in coralline aragonite have been measured by von Allmen et al. (2010), Pretet et al. (2015) and more recently by Hemsing et al. (2018) and Liu et al. (2019), and in coralline high Mg-calcite by Geyman et al. (2019), with all studies reporting enrichment of the lighter isotopes in the solid phase.

In this study, continuing our efforts to deciphering the mechanisms controlling the isotopic fractionation of major and trace elements/impurities in carbonate minerals (e.g. Schott et al., 2016; Mavromatis et al., 2012; 2017c; Oelkers et al., 2018; Saldi et al., 2018; Pearce et al., 2012; Tang et al., 2012; Shirokova et al., 2013), we examine the effect of mineral growth kinetics on Ba isotope fractionation between calcite and aragonite and their forming aqueous solutions. This experimental approach is complemented by first-principles calculations of Ba isotope fractionation at equilibrium. Considering that Ba isotopes in $CaCO_3$ minerals can be used as a proxy tool for their formation in aquatic environments, this study allows for a systematic assessment of the Ba isotopic fractionation in natural carbonates and provides insights on the role of precipitation rates.

2. Material and methods

2.1 Seed materials

The calcite powder used in this study, purchased from Sigma-Aldrich, was pure calcite and contained about 20 μg kg^{-1} Ba. The size of calcite crystals ranged between 2 and 10 μm and their specific area, as determined by the BET method (Brunauer et al., 1938) using krypton and 11 measured adsorption points, was equal to 0.16 m^2 g^{-1}. Aragonite seeds were synthesized at 80 ±2°C by the dropwise addition of 80 mL of a 1.25 M Na_2CO_3 solution into a 2 L borosilicate reactor containing 1.5 L of a 0.1 M $CaCl_2$, 0.1 M $MgCl_2$ and 0.43 M NaCl solution, which was stirred at 240 rpm. The precipitated solids were rinsed with ultrapure water and dried in an oven at 40°C overnight. X-ray diffraction of the synthesized solids showed only the presence of aragonite; the solids Ba content as determined by wet chemical analysis of digested solid using an Inductive Coupled Plasma Optical Emission Spectrometer (PerkinElmer Optima ICP-OES 8300 DV) was equal to ~ 3.5 mg kg^{-1}. Aragonite crystals, 5-20 μm in size, showed characteristic acicular forms. The specific surface area of the synthetic aragonite powder was 0.7 m^2 g^{-1}.

2.2. Experimental set up

Barium co-precipitation experiments with calcite and aragonite were performed using mixed flow reactors as described in Mavromatis et al. (2018). Briefly, mineral overgrowth on $CaCO_3$ seeds under 1 bar pCO_2 was induced by the simultaneous addition of two solutions in a thermally-controlled 1L polypropylene reactor containing the seed material and a background electrolyte of known concentration. The first inlet solution contained $CaCl_2$, $BaCl_2$, and, in experiments conducted in the presence of aragonite seeds, 0.05M $MgCl_2$, whereas the second inlet solution contained Na_2CO_3 in a concentration equal to that of $CaCl_2$ in the first inlet solution. These inlet solutions were added with the aid of a peristaltic pump at equal rates in a reactor containing 0.5 L of a solution that was pre-equilibrated with calcite or aragonite at 1 atm pCO_2. The reactor was equipped with a Teflon floating stir bar rotating at 350 rpm. Shortly prior to each experimental run a small amount of a $BaCl_2$ stock solution (~0.5 mL) was added together with a known amount of seed material in the reactor solution to bring its concentration to ~0.1 mM Ba. In experiments conducted in the presence of calcite, the background electrolyte was 300 mM NaCl, whereas in experiments conducted in the presence of aragonite the background electrolyte consisted of 250 mM NaCl and 25 mM $MgCl_2$. In all experimental runs Ba in both the inlet and reactor solutions originated from a single source of 0.2 M $BaCl_2$ stock solution. The pH of the reactive solution was controlled by the continuous bubbling of a water saturated 1 bar

pCO_2 gas and the measured pH value during the whole course of an experiment was 6.3 ±0.1. In order to minimize evaporation, for all runs CO_2 gas was bubbled in a 300 mM NaCl solution prior to its introduction into the reaction vessel. During the course of a run, the introduction of the two inlet solutions induced an increase of the volume of the reactive solution. Thus, every 24 hours, a volume of reactive fluid, equal to the sum of the volumes of the inlet solutions added in 24 h by the peristaltic pump, was sampled from the reactor so that the fluid volume in the reactor remained constant to within ± 4%. Stirring was stopped shortly prior to sampling to allow the solid material to settle. In this way solid removal was minimized and the solid/fluid ratio was kept quasi constant during the course of an experiment. Immediately after sampling, the fluid was filtered through a 0.2 μm VWR cellulose acetate membrane filter and a sub-sample was acidified for cation concentration analyses. Reactive fluid carbonate alkalinity was determined in a second sub-sample, whereas the fluid pH was measured in-situ. At the end of the experimental run, the entire reactive solution was vacuum filtered through a 0.2 μm membrane filter (Sartorius, cellulose acetate). The solids were rinsed with deionized water and dried at room temperature.

2.3. Chemical and mineralogical analyses

The concentrations of cations in the sampled fluids were measured by Inductive Coupled Plasma Optical Emission Spectrometry (PerkinElmer Optima ICP-OES 8300 DV) with an analytical precision of ± 3% (2sd) determined based on replicate analyses of NIST 1640a and seawater standards. The alkalinity was determined by standard acid titration with an uncertainty of ± 2% using an automated Schott TitroLine alpha plus titrator together with a 10 mM HCl solution. The pH was measured with a Schott Blueline 28 combined electrode, calibrated with standard buffers at pH of 4.01, 7.00 and 10.00 (25°C) with an uncertainty of ±0.03 units. Seed materials and recovered solids were characterized for their X-ray powder diffraction (XRD) patterns. Those were recorded on a PANalytical X´Pert PRO diffractometer using Co-Kα-radiation (40mA, 40kV) at a 2θ range from 4° to 85° and a scan speed of 0.03° s^{-1}. Additionally, selected precipitates were gold-coated and imaged using a ZEISS DSM 982 Gemini scanning electron microscope (SEM) operated at 5 kV accelerating voltage. Specific surface area of seed materials and solids at the end of the experimental runs were determined by the BET method. The bulk chemical composition of the solids at the end of every experimental run was defined after digestion using 3M HNO_3 (Suprapur) and subsequent solution analysis as described above. Finally aqueous speciation of the reactive solutions was calculated using the PHREEQC software together with its MINTEQ.V4 database (Parkhurst and Appelo, 1999).

2.4. Barium isotope analyses

Barium isotope analyses were conducted at the Institut de Physique du Globe de Paris. Between about 2 and 100 mg of solid samples were weighted and dissolved in 3 M HCl to obtain at least 1 µg Ba per sample. An adequate amount of ^{130}Ba-^{135}Ba double spike (van Zuilen et al. 2016) was added to the dissolved samples. For solution samples, aliquots of around 150 µl were directly mixed with the double spike. All samples were taken to dryness and re-dissolved in 3 M HCl for ion-exchange chromatography. The chromatographic protocol is based on the one by van Zuilen et al. (2016), but acid strengths were adapted to 3 M HCl for matrix removal (7 ml in total) and 6 M HCl for Ba collection (6 ml). Total procedure blanks were below 0.2 ng.

Isotope measurements were done on a Thermo Scientific Neptune Plus MC-ICP-MS. The dried samples were diluted in 0.5 M HNO_3 to 300 µg kg^{-1} natural Ba. Solutions were introduced into the mass spectrometer via a quartz dual cyclonic spray chamber. Typical $^{137}Ba^+$ signals were ~3.5 V (using a 10^{11} Ω resistor). Data acquisition was performed in low-resolution mode and consisted of 100 cycles of 4 s integration time. Signals of all seven Ba isotopes were detected simultaneously with $^{129}Xe^+$ and $^{131}Xe^+$ to correct for isobaric interferences on ^{130}Ba, ^{132}Ba, ^{134}Ba and ^{136}Ba. All isotope data are given relative to the reference material NIST SRM 3104a in the $\delta^{137/134}Ba$ notation (in ‰):

$$\delta^{137/134}\mathrm{Ba} = \left[\frac{(^{137}\mathrm{Ba}/^{134}\mathrm{Ba})_{\mathrm{sample}}}{(^{137}\mathrm{Ba}/^{134}\mathrm{Ba})_{\mathrm{SRM\ 3104a}}} - 1\right] \times 1000 \qquad (1)$$

SRM 3104a was measured after every second sample. After double-spike deconvolution of the raw data (van Zuilen et al., 2016), the $\delta^{137/134}Ba$ values of SRM 3104a usually deviated from zero by up to 0.16 ‰. As no drift was observed during an analytical session, the $\delta^{137/134}Ba$ values of the samples were normalised to the daily average $\delta^{137/134}Ba$ value of SRM 3104a. The intermediate measurement precision was estimated by calculating the pooled 2 standard deviation ($2s_p$) of the sample data set according to

$$s_p = \sqrt{\frac{\sum_{i=1}^{k}(n_i-1)s_i^2}{\sum_{i=1}^{k}(n_i-1)}}, \qquad (2)$$

where n_i is the number of repeated measurements of each sample i and s_i^2 their variance, to be ±0.039 ‰ (n=53). Sample data are reported with either the $2s_p$ uncertainty or the 2 standard deviation (2sd) of the repeated analyses (Table 1) if the latter is larger than 0.039 ‰. Analytical accuracy was assessed by repeated analyses of the in-house standards BaBe12 (-1.130 ± 0.045 ‰, n = 3) and BaBe27 (-0.610 ± 0.034 ‰, n = 10), which are in good agreement with literature values (van Zuilen et al., 2016).

2.5 Description of isotope fractionation as a function of the reaction rate within the framework of Transition State Theory

For a slow elementary reaction to proceed, the reactant species have to pass a potential energy barrier which is a configuration roughly midway between that of the reactants and the products. Transition state theory (TST) originally developed by Eyring (1935) provides the means to characterize the path of reactants over this energy barrier and their configuration, often termed the activated complex, in the neighborhood of this energy maximum. According to TST, the rate of an elementary reaction depends on the number of reactants that cross the energy barrier and the time needed for these complexes to yield products. Within this concept the rate of a forward elementary reaction R_f can be written:

$$R_f = k^* [AC^*] \tag{3}$$

where k^* refers to a rate constant and $[AC^*]$ stands for the concentration of the activated complex. The same approach can be applied to a reversible chemical reaction leading to the formation of component XYZ from reactants X and YZ

$$\mathrm{X} + \mathrm{YZ} \rightleftharpoons \mathrm{XYZ}\ ,\ \ K \tag{4}$$

where K stands for the equilibrium constant of reaction (4). Element X contains two isotopes, heavy ^{h}X and light ^{l}X. Therefore the potential energy barrier the reactants have to pass for forming light ^{l}XYZ is lower than that for heavy ^{h}XYZ. The forward formation reaction of ^{l}XYZ can be described by

$$^{l}X + YZ \rightleftharpoons {}^{l}XYZ^* \quad , {}^{l}K_f^*$$

$$(5)$$

$$^{l}XYZ^* \rightarrow {}^{l}XYZ$$

where the activated complex $^{l}XYZ^*$ is assumed to be in equilibrium with ^{l}X and YZ, and $^{l}K_f^*$ is its formation constant. The rate of reaction (5), $^{l}R_f$, can be expressed as

$$^{l}R_f = {}^{l}k_f^* \, [{}^{l}XYZ^*] = {}^{l}k_f^* \; {}^{l}K_f^* \, [{}^{l}X].[YZ] = {}^{l}k_f \, [{}^{l}X].[YZ] \qquad (6)$$

and the rate of the backward reaction

$$^{l}XYZ \rightarrow {}^{l}X + YZ \qquad (7)$$

is given by

$$^{l}R_b = {}^{l}k_b^* \, [{}^{l}XYZ^*] = {}^{l}k_b^* \; {}^{l}K_b^* \, [{}^{l}XYZ] = {}^{l}k_b \, [{}^{l}XYZ] \qquad (8)$$

with $^{l}k_f / {}^{l}k_b = {}^{l}K$, where ^{l}K is the formation constant of ^{l}XYZ and $^{l}R_{net} = {}^{l}R_f - {}^{l}R_b$ is the overall rate of formation of ^{l}XYZ. An equation similar to eq. (8) can be written for the formation of heavy ^{h}XYZ. The two kinetic isotopic fractionation factors associated with the forward and backward reactions are given by $\alpha_f = {}^{h}k_f / {}^{l}k_f$ and $\alpha_b = {}^{h}k_b / {}^{l}k_b$ whereas the equilibrium fractionation factor is $\alpha_{eq} = \alpha_f / \alpha_b = {}^{h}K / {}^{l}K$.

Introducing the Gibbs free energy change for the formation reaction, yields the following relation for the overall rate of formation of ^{l}XYZ and ^{h}XYZ

$$^{l}R_{net} = {}^{l}k_f (1 - \exp({}^{l}\Delta G / RT)) \qquad (9)$$

$$^{h}R_{net} = {}^{h}k_f (1 - \exp({}^{h}\Delta G / RT)) \qquad (10)$$

whereas the overall rate of reaction (4) is given by

$$R_{\mathrm{net}} = {}^{1}R_{\mathrm{net}} + {}^{\mathrm{h}}R_{\mathrm{net}} = k_{\mathrm{f}}(1 - \exp(\Delta G/\mathrm{R}T)) \qquad (11)$$

where k_{f} and ΔG stand for the forward rate constant and Gibbs free energy change.

Introducing $\mathrm{r_r} = [{}^{\mathrm{h}}\mathrm{X}]/[{}^{\mathrm{l}}\mathrm{X}]$ and $\mathrm{r_p} = [{}^{\mathrm{h}}\mathrm{XYZ}]/[{}^{\mathrm{l}}\mathrm{XYZ}]$, the isotope ratio in the reactant and product, respectively, two equations can be derived from eqs (6) and (8) that relate the two isotope- forward and backward reaction rates:

$${}^{\mathrm{h}}R_{\mathrm{f}} = \alpha_{\mathrm{f}}.\mathrm{r_r}.{}^{\mathrm{l}}R_{\mathrm{f}} \qquad (12)$$

and

$${}^{\mathrm{h}}R_{\mathrm{b}} = (\alpha_{\mathrm{f}}/\alpha_{\mathrm{eq}})\mathrm{r_p}.{}^{\mathrm{l}}R_{\mathrm{b}} \qquad (13)$$

The expression of the fractionation factor between the products and the reactants at a given time can be derived from eqs (12) and (13):

$$\alpha = \alpha_{eq}\frac{{}^{l}R_{f}.\,{}^{h}R_{b}}{{}^{l}R_{b}.\,{}^{h}R_{f}} \qquad (14)$$

At steady-state, which corresponds to a constant isotope composition of XYZ as a function of time, it can be shown that $r_p = \frac{{}^{h}R_{net}}{{}^{l}R_{net}}$. Substitution of eqs (12) and (13) into this relation leads after some algebraic handling to the following expression of the isotope fractionation factor at steady-state:

$$\alpha_{SS} = \frac{\alpha_f}{1+\frac{{}^{l}R_b}{{}^{l}R_f}\left(\frac{\alpha_f}{\alpha_{eq}}-1\right)} = \frac{\alpha_f}{1+\frac{{}^{l}R_b}{{}^{l}R_{net}+\,{}^{l}R_b}\left(\frac{\alpha_f}{\alpha_{eq}}-1\right)} \qquad (15)$$

At equilibrium, $\alpha_{ss} = \alpha_{eq}$ and $\frac{{}^{l}R_b}{{}^{l}R_f} = \frac{R_b}{R_f} = 1$. At kinetically controlled conditions with $R_{net} > R_b$ and $\alpha_{ss} \sim \alpha_f$, the ratios $\frac{{}^{l}R_b}{{}^{l}R_f}$ and $\frac{R_b}{R_f}$ can be considered to be equal because for most geochemical reaction α_{eq} and α_f differ only by a few per mil. As such eq. (15) simplifies to

$$\alpha_{ss} = \frac{\alpha_f}{1 + \frac{R_b}{R_{net}+R_b}\left(\frac{\alpha_f}{\alpha_{eq}} - 1\right)} \tag{16}$$

Equation (16) is identical to the eq. (11) derived by DePaolo (2011) to describe the steady-state calcium isotope fractionation during calcite precipitation, assuming the precipitation of this mineral follows the first order TST rate law. In this equation R_b and R_{net} stand for calcite backward dissolution rate and net precipitation rate, respectively, whereas α_f represents the kinetic isotope fractionation factor associated with calcite precipitation. Eq. (16) can be also applied to describe the isotope fractionation of a trace metal like barium during its steady-state coprecipitation with calcite or aragonite. Indeed, considering that the substitution of a trace metal for Ca in $CaCO_3$ leads to the formation of a true $Ca_{1-x}Me_xCO_3$ solid solution, it should be noted that at steady-state precipitation the chemical composition of the precipitating solid does not change with time and therefore the precipitation rate of Me_xCO_3 is equal to that of the $Ca_{1-x}Me_xCO_3$ solid solution. The above TST rate laws have been derived for an element containing only two isotopes. It should be noted, however, that eq. (16), that describes the fractionation factor at steady-state conditions, can be as well applied to an element like Ba containing several isotopes to account for the steady-state behaviour of any stable isotope couple like $^{137/134}$Ba or $^{138/134}$Ba. In the following, eq. (16) has been therefore used to describe the value of α_{ss} for

$^{137/134}$Ba as a function of calcite or aragonite net precipitation rate (R_{net}) during the steady-state co-precipitation of barium with calcite or aragonite.

2.6. First-principles calculation of equilibrium Ba isotope fractionation

The investigated models of Ba-bearing calcite and aragonite are based on the 2 × 2 × 2 rhombohedral calcite supercell and the 2 × 1 × 2 orthorhombic aragonite supercell in which one Ba atom is substituted for one Ca atom. Both supercells contain a total of 80 atoms. The Ba atom is separated from its periodic images by ~ 8 Å in the shortest direction of the aragonite model and by at least 10 Å in the calcite model. We can thus consider the Ba atom as isolated and models as representative of the dilute samples studied here. The pure barium carbonate (witherite, $BaCO_3$) was also modeled. In order to approach the structure of an Ba aquo ion, we took the crystal structure of barium hydroxide octahydrate ($Ba(H_20)_8(OH)_2$) described by Persson et al. (1995). This approach was chosen because modeling of Ba aquo ion using *ab initio* molecular dynamic simulations is not expected to change significantly the results and such approach would represent an extensive theoretical study on its own.

According to Bigeleisen and Mayer (1947), the equilibrium isotopic fractionation factor (α) between two phases (a and b) can be determined from the reduced partition function ratios (β):

$$\alpha(a,b) = \beta(a)/\beta(b) \tag{17}$$

more conveniently expressed in ‰ with the following logarithmic relation:

$$1000ln\alpha(a,b) = 1000ln\beta(a) - 1000ln\beta(b) \tag{18}$$

Since the equilibrium mass-dependent isotopic fractionation arises mainly from the change in vibrational energy induced by the isotopic substitution, the β-factor can be calculated from the harmonic vibrational frequencies as follows (e.g. Blanchard et al., 2017):

$$\beta = \left[\prod_{i=1}^{3N_{at}} \prod_{\{q\}} \frac{\nu_{q,i}^{*}}{\nu_{q,i}} \frac{e^{-h\nu_{q,i}^{*}/(2kT)}}{1-e^{-h\nu_{q,i}^{*}/(kT)}} \frac{1-e^{-h\nu_{q,i}/(kT)}}{e^{-h\nu_{q,i}/(2kT)}}\right]^{1/(nN_q)} \qquad (19)$$

where $\nu_{q,i}$ and $\nu_{q,i}^{*}$ are the frequencies of the vibrational mode defined by indexes i (i=1,3N_{at}) and wavevector q for the two isotopically distinct systems. N_{at} is the total number of atoms in the simulation cell, N_q the number of wavevectors, n the number of isotopically exchanged sites (1 for calcite and aragonite, 4 for witherite and the hydrate), h Planck's constant, k Boltzmann's constant, T the temperature. The second product is performed on a sufficiently large grid of N_{q} wavevectors in the Brillouin zone.

The structural relaxations (*i.e.* optimization of atomic positions and cell parameters) followed by the vibrational frequency calculations were carried out from first-principles calculations based on density functional theory, using the PWscf and PHonon codes of the Quantum ESPRESSO package (Giannozzi et al., 2009; http://www.quantum-espresso.org). The computational parameters used here are similar to the ones used in previous works on sulfate-bearing calcium carbonates (Balan et al., 2014), on Mg-bearing carbonates (Pinilla et al., 2015), and on boron-bearing carbonates (Balan et al., 2016; 2018). Namely, we used the generalized gradient approximation (GGA) to the exchange-correlation functional with the Perdew-Burke-Ernzerhof (PBE) parametrization (Perdew et al., 1996). The ionic cores of all elements (Ba, Ca, C, O, H) were described by ultrasoft pseudopotentials from the GBRV library (Garrity et al., 2014). The electronic wave functions and charge density were expanded using finite basis sets of plane-waves with 60 and 300 Ry cutoffs respectively. Electronic integration is performed by sampling the Brillouin zone according to the Monkhorst-Pack scheme (Monkhorst and Pack, 1976) with a 3 × 2 × 3 shifted *k*-point grid for witherite, and a 2 × 2 × 2 shifted *k*-point grid for the three other phases (calcite, aragonite and barium hydroxyl hydrate). These values lead to a convergence of the total energy better than 0.5 mRy/atom. Structural relaxations were performed until the residual forces on atoms were less than 5.10^{-5} Ry/a.u., before computing the harmonic frequencies on a 2 × 1 × 2 shifted grid of wavevectors for witherite, and on a single shifted wavevector for the three other phases.

3. Results

3.1 Composition and precipitation rates of $CaCO_3$ overgrowths.

As mentioned earlier by Mavromatis et al. (2018), the XRD patterns of collected solids are indicative of calcite or aragonite and they do not exhibit differences with those of the seed material. It is worth noting, however, that three experiments reported in this study exhibit peaks of both calcite and aragonite despite the fact that the seed material was aragonite. Based on Rietveld refinement analyses using the PANalytical X'Pert HighScore Plus software coupled with the PDF-2 database, the abundance of aragonite in the bulk precipitate of experiments CaBa38, CaBa39 and CaBa40 was 37.2, 26.5 and 15.4 wt.%, respectively (Table 1). In these experiments growth rate estimation is not straightforward as nucleation of calcite in the reactive fluid produces material with specific surface different than that of aragonite. As such herein we estimated steady-state growth rate as in previous studies (e.g. Mavromatis et al., 2013; 2015;

2017b) based on the number of moles of Ca added to the reactor per time unit corrected for the number of moles of Ca removed from the reactor via sampling:

$$R_{\mathrm{p}} = \frac{n_{\mathrm{Ca(add)}} - n_{\mathrm{Ca(rem)}}}{86{,}400} / S \qquad (20)$$

where 86,400 is the number of seconds in time unit (i.e. 24 h), S is the total surface area of $CaCO_3$ in m^2 and R_p is expressed in $mol/m^2/s$. Similar to the experiments presented in Mavromatis et al. (2018), the total surface area of experiments CaBa38, CaBa39 and CaBa40 has been corrected for the amount of precipitated $CaCO_3$ mineral phase based on steady-state aqueous concentration of Ca. We note however that rate estimation for those three experiments using eq. (20) is based on the assumption that calcite has the same specific surface area as aragonite.

The barium content of the precipitated overgrowths range between 20-50 mg kg^{-1} and 1450-3350 mg kg^{-1} in calcite and aragonite, respectively. The values of corresponding partition coefficients ($D_{Ba} = \frac{(\frac{[Ba]}{[Ca]})_{solid}}{(\frac{[Ba]}{[Ca]})_{fluid}}$) which increases with the overgrowth precipitation rates, range between $0.004 \leq D_{\mathrm{Ba}} \leq 0.009$ and $0.22 \leq D_{\mathrm{Ba}} \leq 0.77$ for calcite and aragonite, respectively (Table 1).

In the CaBa38, CaBa39 and CaBa40 runs, which lead to a mixture of aragonite and calcite in the overgrowths, only a small fraction of barium was incorporated in calcite due to the significant higher affinity of barium for aragonite than for calcite. The fractions of Ba in the solid that was incorporated in calcite in runs CaBa38, CaBa39 and CaBa40 have been estimated to range between 1.4 and 4.5 % of the total amount of Ba in the overgrowth.

3.2 Barium isotope composition of $CaCO_3$ overgrowths

The $\delta^{137/134}$Ba composition of the stock solution used in all the runs had a value of 0.085±0.039 ‰ ($2s_p$; see Table 1). This composition is identical to that of the $BaCl_2$ solution used for the experiments on Ba isotope fractionation between witherite and aqueous solution reported in Mavromatis et al. (2016). Over the course of an experimental run, as well as among runs, the isotopic composition of the reactive fluids shows insignificant variations in $\delta^{137/134}$Ba composition compared to the stock solution as it can be seen in Table 1 for all experiments either the growing mineral was calcite (CaBa5, CaBa8 and CaBa14) or aragonite (CaBa25, CaBa28 and CaBa29).

The $\delta^{137/134}$Ba composition of the six calcite overgrowths analyzed in this study does not exhibit analytically significant variation compared to the $BaCl_2$ stock solution, however precipitates of experiments CaB12 and CaBa14 may be slightly enriched in light isotopes compared to the other samples (by near 0.05 ‰). In contrast, the $\delta^{137/134}$Ba composition of the eleven aragonite overgrowths exhibit significant variations with values ranging from 0.339±0.049 ‰ for experiment CaBa31 to 0.037 ± 0.039 ‰ ($2s_p$) for experiment CaBa30. The three experiments where the overgrowth was a mixture of calcite with aragonite exhibit $\delta^{137/134}$Ba composition that is enriched in the lighter Ba isotopes compared to the stock solution, ranging between 0.032±0.044 ‰ and -0.011±0.068 ‰ (see Table 1).

3.3 Barium isotope fractionation between calcium carbonates and the fluid

The $\Delta^{137/134}Ba_{mineral\text{-}fluid}$ values listed in Table 1 have been deduced from the difference between the isotopic composition of the solid and that of the forming fluid (i.e. $\Delta^{137/134}Ba_{solid\text{-}fluid} = \delta^{137/134}Ba_{solid} - \delta^{137/134}Ba_{fluid}$). This approach has been used because in all runs Ba aqueous concentration in the reactor was the same within uncertainty than that of the inlet solution and $\delta^{137/134}Ba_{fluid}$ did not exhibit temporal variations and was identical within analytical uncertainties among the various runs (see Table 1). For calcite, $\Delta^{137/134}Ba_{calcite-fluid}$ has an average value of -0.003 ±0.040 ‰ and does not exhibit a significant variation with calcite growth rate in the range of growth rates investigated (Fig. 1A). In contrast the $\Delta^{137/134}Ba_{aragonite-fluid}$ values exhibit a systematic decrease as a function of increasing aragonite growth rate (Fig. 1B) that can be described by the following linear trend:

$$\Delta^{137/134}Ba_{aragonite-fluid} = -0.1834\ (\pm 0.0314)\ LogRate - 1.4843\ (\pm 0.2490);\ R^2 = 0.75, \qquad (21)$$

with this relation to be valid for $-9.0 \leq LogRate \leq -7.6$. Note that samples CaB38, CaB39 and CaB40 have been included in this fit as their isotopic composition could not have been impacted by the very small Ba content of the calcite co-precipitated with aragonite. Eq. (21) suggests that aragonite which is formed at low growth rates ($\leq 10^{-8.1}$ mol/m^2/s) is enriched in the heavier Ba isotopes. In contrast at growth rates $\geq \sim 10^{-8.0}$ mol/m^2/s, the forming solid becomes progressively enriched in the lighter Ba isotopes.

3.4 Theoretical structural and isotopic properties

The relaxed cell parameters of barium hydroxide octahydrate (a = 9.296 Å, b = 9.288 Å, c = 11.884 Å, β = 99.17) are in good agreement with the experimental structure (Persson et al. 1995); the theoretical volume being only 0.3% larger than the experimental one. In this model, the eight water molecules of the first solvation shell are at an average distance of 2.84 Å from Ba^{2+}. Keeping in mind that the first atomic neighbors greatly influence the equilibrium isotopic fractionation, we can expect this hydrate to be a good analogue of an aqueous Ba^{2+} ion. Indeed, extended X-ray absorption fine structure (EXAFS) spectroscopy studies of dilute aqueous solutions report a hydration number of about eight (8.1 and 7.8) and average Ba-O bond length of 2.81 and 2.78 Å (Persson et al. 2015 and D'Angelo et al. 1996, respectively). The three carbonate minerals (witherite, pure calcite and pure aragonite) show calculated cell parameters about 1% larger than the experimental values. The small overestimation is typical of the GGA functional used. The average Ba-O distances in witherite, aragonite and calcite are 2.85, 2.75 and 2.67 Å, respectively. For comparison, the crystal structure refinement gives 2.81 Å for witherite where Ba has a coordination number of 9 (de Villiers, 1971). X-ray absorption spectroscopy measurements on a Ba substituted calcite (~2000 mg kg^{-1} Ba) give a Ba-O bond length of 2.68 Å with a coordination number of 6 (Reeder et al., 1999). As for aragonite, there is no available data in either synthetic or natural aragonite (e.g. Ba concentrations in corals are too low for EXAFS analyses; Finch et al., 2010). However, it has been found that Sr and Mg are in 9-fold coordination with respect to O in the aragonite lattice (Finch and Allison, 2007).

The temperature dependence of β-factors is shown in Fig. 2 and the corresponding polynomial fits are given in Table 2. Results indicate that at equilibrium, calcite and in particular aragonite will be enriched in the heavy Ba isotopes relative to aqueous barium, whereas no fractionation is expected between witherite and aqueous barium. At 25°C, the theoretical equilibrium fractionation factors $1000\ln\alpha_{\text{mineral-fluid}}$ are +0.34‰, +0.17‰ and -0.01‰ for aragonite, calcite and witherite, respectively. This latter value between witherite and aqueous Ba is consistent with the experimentally derived fractionation factor of -0.07 ± 0.04‰ (Mavromatis et al., 2016). It is noteworthy that in the present case, the relative order of heavy isotope enrichment (Ba hydrate < calcite < aragonite) does not follow the usual anticorrelation with the average bond length (Ba-hydrate with 2.84 Å > aragonite with 2.75 Å > calcite with 2.67 Å). This observation may be explained by the contrasted Ba local environments in calcite and aragonite (Fig. 3). While there are six carbonate groups around the Ba atom in both minerals, these groups are arranged differently. In calcite, carbonate groups are located in two crystallographic planes and the six Ba-O bonds have the same length. In aragonite, carbonate groups belong to four crystallographic planes and the Ba atom forms one or two bonds with each carbonate group, leading to a coordination number of 9. The effect of this local environment on the barium atom is expressed through the interatomic force constant (Fig. 4). The Ba force constant is 19% larger in aragonite than in calcite, and therefore an aragonite crystal will be enriched in heavy Ba isotopes if in thermodynamic equilibrium with a calcite crystal.

4. Discussion

4.1 The impact of calcite and aragonite growth kinetics on Ba isotope fractionation

During the standard growth mechanism of carbonate minerals involving ion-by-ion attachment to advancing steps, desolvation of the metal ion and thus the rate of exchange of water molecules in its coordination sphere are believed to control the incorporation of the metal in the crystal lattice (Pokrovsky and Schott, 2002; Hofmann et al., 2012). For instance, it has been found experimentally that (de)solvation processes seem to substantially impact Ba isotope fractionation upon mineral formation (Böttcher et al., 2018a). As water exchange rate in the hydration shell follows an inverse power-law mass dependence (Hofmann et al., 2012), light isotopes are preferentially incorporated into the precipitating solid and the resulting kinetic fractionation should increase with increasing precipitation rate. Equation (16) shows that for steady-state precipitation this kinetic effect is maximum at conditions where the net precipitation rate is much faster than the dissolution rate whereas it is null at chemical equilibrium (equality of the forward and backward reaction rates). This increasing enrichment of the solid in light isotopes with precipitation rate has been observed for calcium in calcite (Tang et al., 2008a), magnesium in magnesite (Pearce et al., 2012), barium in witherite (Mavromatis et al., 2016; Böttcher et al., 2018b) and strontium in strontianite (Mavromatis et al., 2017a). It is expected that the isotopic composition of the divalent metals substituted for Ca in the $CaCO_3$ lattice should follow a similar dependence on growth rate provided that the desolvation rates of these metals are comparable to that of calcium. This is indeed observed for example during the incorporation of Sr in calcite (Boehm et al., 2012) and Ba in aragonite (this study), two alkaline earth metals with water-exchange rates in their coordination sphere ($10^{-8.9}$ and $10^{-9.2}$ s^{-1}, respectively; Lincoln and Merbach, 1995) very close to that for calcium ($10^{-8.8}$ s^{-1}; Lincoln and Merbach, 1995). However, the isotopic composition of Ba during its incorporation in calcite does not exhibit a significant dependence on calcite growth kinetics for the range of precipitation rates investigated in the present study ($10^{-7.3}$-$10^{-8.0}$ mol m^{-2} s^{-1}). It is tempting to use eq. (16) derived from TST to try to understand the apparent contrasting behaviour of Ba isotope fractionation during calcite and aragonite steady-state precipitation.

The application of eq. (16) to Ba isotope fractionation in aragonite is shown in Fig. 5A. For this calculation, a constant value of aragonite backward dissolution rate, $R_b = 1\times10^{-7}$ mol m^{-2} s^{-1} at 25°C and pH = 6.25, is assumed based on the R_b value determined in pure water by Chou et al. (1989) corrected for the inhibiting effect of aqueous Mg (25 mM $MgCl_2$ in the background electrolyte) on aragonite dissolution rate as quantified by Gutjar et al. (1996). A good fit of the experimental data is obtained using values of $\alpha_{eq} = 1.00027$ ($\Delta^{137/134}Ba_{aragonite\text{-}fluid}(eq) = +0.27\pm0.06‰$) and $\alpha_f = 0.9980\pm0.0002$ ($\Delta^{137/134}Ba_{aragonite\text{-}fluid}(kin) = -2.0\pm0.2‰$). For this fit the value of α_{eq} in eq. (16) is kept constant and that of α_f is allowed to achieve minimum and maximum values in the growth rate range where experimental data occur. It should be noted that the value of the kinetic fractionation factor used is this study is slightly lower than that proposed by Hofmann et al. (2012) based on MD simulations ($\alpha_f = 0.9989$). The good fit of Ba isotope data by eq. (16) is noteworthy because the selected aragonite R_b value is not an adjustable parameter and the α_{eq} value that fits the data best is in excellent agreement with the fractionation measured at the slowest aragonite growth rates (10^{-9} mol m^{-2} s^{-1}). This experimental model is also strengthened by the comparison with first-principles calculations. The equilibrium fractionation factor derived here (+0.27±0.06‰) is in good agreement with the theoretical value (+0.34‰). Interestingly the model predicts that significant kinetic fractionation of Ba isotopes ($\Delta^{137/134}Ba_{aragonite\text{-}fluid} < -1$ ‰) should be observed for very fast aragonite growth rate ($R_p > 10^{-7}$ mol m^{-2} s^{-1}), similar to those met during the growth of biominerals such foraminifera and corals (e.g. Gussone et al., 2005; Lorrain et al, 2005). Furthermore, the TST kinetic model confirms that, depending on the value of aragonite growth rate, Ba isotope fractionation between aragonite and its forming fluid could be positive at near thermodynamic equilibrium but also negative or equal to zero under mineral formation from an oversaturated fluid with respect to aragonite.

The application of eq. (16) to Ba isotope fractionation during steady state calcite precipitation is shown in Fig. 5B. With a value of calcite backward dissolution rate equal to 2×10^{-6} mol m^{-2} s^{-1} at 25°C and pH = 6.2 (Chou et al., 1989), the dashed line in Fig. 5B is obtained for limiting fractionation factors of $\alpha_{eq} = 1.00002$ ($\Delta^{137/134}Ba_{calcite\text{-}fluid}(eq) = +0.02\pm0.06$ ‰) and $\alpha_f = 0.9982\pm0.0002$ ($\Delta^{137/134}Ba_{calcite\text{-}fluid}(kin) = -1.8 \pm 0.2$‰). In contrast with witherite and aragonite, we note for calcite a small but significant discrepancy between experimental and theoretical equilibrium fractionation factors (+0.02‰ against +0.17‰). The model which accurately accounts for the very small Ba isotope fractionation observed also indicates that calcite growth rates investigated in the present study ($R_p \leq 5\times10^{-8}$ mol m^{-2} s^{-1}) were too slow to induce substantial kinetic isotope fractionation. Fig. 5B shows that kinetic Ba isotope fractionation greater than -1‰ should be observed for calcite growth rates ≥ 10^{-6} mol m^{-2} s^{-1} which is consistent with available data on Ca and Sr isotopes fractionation during calcite growth which show substantial kinetic fractionation of – 1.5‰ (Ca) and – 0.3‰ (Sr) for calcite growth rates of ~3×10^{-6} mol m^{-2} s^{-1} (Tang et al., 2008a; Boehm et al., 2012).

4.2 Control of Ba equilibrium isotope fractionation during co-precipitation with aragonite and calcite.

Calcite. The equilibrium value for $\Delta^{137/134}Ba_{calcite-fluid}$(eq) determined in this study (+ 0.02‰) suggests that at equilibrium no significant Ba isotope fractionation occurs between calcite and solution. This result is in contradiction with DFT predictions. The Ba isotope composition in calcite measured in this study thus does not seem consistent with the rule governing mass-dependent isotope fractionation stating that, at equilibrium, the heavy isotopes of an element will tend to be concentrated in substances where that element forms the stiffest bonds (Schauble, 2004; Blanchard et al., 2017). The apparent discrepancy and the lack of Ba isotope fractionation during Ba co-precipitation with calcite likely originates from the mechanism of incorporation of this element in the growing crystal. In the standard calcite growth under low saturation state conditions, the first step is the ion-by-ion attachment of reacting species, including Ca and Ba aquo ions to the crystal advancing steps. During this sorption step, Ba forms with a calcite surface CO_3 group a monodendate inner sphere complexes in which a CO_3 substitutes for a water molecule of Ba coordination sphere (Pokrovsky et al., 2000). This surface complex, in which Ba likely keeps the same coordination (8) and undergoes only subtle change of its first hydration shell (replacement of a H_2O by a CO_3), is not expected to have an isotopic composition which differs significantly from that of the Ba aquo ion (Saldi et al., 2018). The following Ba incorporation in calcite lattice and substitution for Ca is accompanied by a reduction of Ba coordination number and average Ba-O bond length to 6 and ~2.68 Å, respectively. This structural change must occur without further exchange with Ba in solution as the experiments do not document significant Ba isotope fractionation between calcite and the fluid. Such a mechanism has already been invoked to explain the isotopic composition of boron (Sen et al., 1994; Noireaux et al., 2015; Balan et al., 2018) and zinc (Mavromatis et al., 2019) co-precipitated with calcite.

Aragonite. Ba co-precipitation with aragonite is accompanied by a significant enrichment of the solid in ^{137}Ba at equilibrium with $\Delta^{137/134}Ba_{aragonite\text{-}fluid}(eq) = +0.27‰$. This value is in good agreement with the theoretical one (+0.34‰). The incorporation of the Ba aquo ion in the aragonite lattice does not require a significant change in its coordination number. This positive fractionation is related to the reduction of the average Ba-O bond length (from 2.84 Å in the aqueous ion to 2.75 Å in the aragonite), which is induced by structural constraints imposed by the surrounding $CaCO_3$ structure. To our knowledge this is the first time that is reported the enrichment of an alkaline earth in heavy isotopes during its incorporation in a carbonate mineral. All previous experimental studies have reported the enrichment in light isotopes of Ca, Mg, Sr and Ba in carbonate minerals (e.g. Tang et al., 2008a; Oelkers et al., 2019; Boehm et al., 2012; Böttcher, 2012; 2018a; 2018b; Pearce et al., 2012; Mavromatis et al., 2013; 2016; 2017c; Immenhauser et al., 2010; Li et al., 2012; 2015; von Allmen et al., 2010).

4.3 Implications for the use of Ba isotopes in natural $CaCO_3$ minerals

The most interesting feature observed in the experimental results of this study is the fact that the $\Delta^{137/134}Ba_{aragonite\text{-}fluid}$ can present both positive and negative values, depending on the growth rate at which aragonite forms. In addition to this observation, the theoretical modelling of the experimental findings suggests that growth rate can induce variations to the fractionation factor between aragonite and fluid as large as -2.0 ‰ (see Fig. 5A). To date the Ba isotope data in natural aragonites are limited to three studies and are derived exclusively from aragonitic corals (Pretet et al., 2015; Hemsing et al., 2018; Liu et al., 2019). In these studies, the fractionation factors between Ba in the coral and seawater are reported to range between -0.15 and -0.3‰, however the interpretation of these variations when present is assigned to vital effects (see Pretet et al., 2015) and is not taking into account growth rate effects. According to the TST fit described in Fig. 5 using eq. (16), these fractionation factors can be the result of relatively fast aragonite growth rates ranging from $10^{-7.7}$ to $10^{-7.4}$ mol m^{-2} s^{-1}. Such fast aragonite growth rate would as well impact the Ba partition coefficient between aragonite and the fluid (Mavromatis et al., 2018) and suggest co-variation in Ba concentration and Ba isotope composition in natural aragonitic samples such as corals. Considering however that vital effects as well as the presence of pure $BaCO_3$ in the coralline aragonite skeletons (Liu et al., 2019) can affect their Ba isotope composition, direct use of this isotopic system for growth rate estimates may be challenging. On the other hand, the formation of speleothems commonly occurs at low growth rates. The positive $\Delta^{137/134}Ba_{aragonite\text{-}fluid}$ values at low growth rates of aragonite, and the ability for robust estimation of growth rate in speleothem aragonite suggests that the chemical and isotopic composition of Ba in the solid phase can provide information for the composition of the fluid from which they were formed.

With respect to the application of Ba isotope fractionation in natural aragonitic archives, an interesting implication is the negative relationship of the partition coefficient and isotope fractionation of Ba between aragonite and the precipitating fluid that can be numerically described using the linear equation:

$$\Delta^{137/134}\mathrm{Ba}_{\text{aragonite-fluid}} = -0.5783 \times \mathrm{Log}D_{\mathrm{Ba}} - 0.134 \; (R^2 = 0.84) \qquad (22)$$

and is valid for $-0.11 \leq \mathrm{Log}D_{\mathrm{Ba}} \leq -0.66$. As it can be seen in Fig. 6, at near chemical and isotopic equilibrium conditions, $\Delta^{137/134}\mathrm{Ba}_{\text{aragonite-fluid}}$ attains its maximum value of about +0.3‰, whereas D_{Ba} approaches its minimum value of ~ $10^{-0.7}$. The advantage of the relationship between Ba chemical partitioning and isotopic fractionation that is described with eq. (22) is that it is independent of the precipitation rate of aragonite, thus it can be used as a multiproxy approach to decipher variations of chemical and isotopic composition of the forming fluid. Similar approach has been used earlier based on Sr incorporation and Ca isotope fractionation during calcite formation (Tang et al., 2008a). In the case of Ba in aragonite, if the $(\mathrm{Ba/Ca})_{\mathrm{aq}}$ ratio of the aragonite forming fluid is known and can be considered to be constant during mineral growth, the $D_{\mathrm{Ba,aragonite}}$ value is determined by analysing the Ba content of the precipitated aragonite. This $D_{\mathrm{Ba,aragonite}}$ value is defining the $\Delta^{137/134}\mathrm{Ba}_{\text{aragonite-fluid}}$ with the aid of eq. (22). Thus, the obtained $\Delta^{137/134}\mathrm{Ba}_{\text{aragonite-fluid}}$ values can be used for the reconstruction of the Ba isotopic composition of the fluid present during aragonite formation by analyzing the Ba isotopes of the aragonite, regardless of precipitation rates. However, further systematic experiments are required to get distinct insight into the impact of decisive environmental factors, like ionic strength, Mg/Ca ratio, temperature and Ba speciation in the fluid phase on Ba distribution and isotope fractionation during aragonite formation.

Finally, another important finding of this study is the absence of significant Ba isotope fractionation during calcite standard inorganic growth mechanism at near equilibrium conditions despite Ba coordination number and Ba-O bond lengths are notably reduced in calcite compared to the Ba aquo ion. This likely arises because the structural change accompanying adsorbed Ba incorporation in the crystal lattice occurs without exchange between aqueous and solid barium.

5. Conclusions

Based on laboratory experiments and first-principles calculations, we have investigated the Ba isotope fractionation between the anhydrous $CaCO_3$ minerals, calcite and aragonite, and reactive fluids. In the case of calcite, experimental results show an almost insignificant Ba isotope fractionation ($\Delta^{137/134}Ba_{calcite\text{-}fluid}$ = +0.02±0.06‰) and indicate a weak impact of growth rate on the $\Delta^{137/134}Ba_{calcite\text{-}fluid}$ within the range of mineral growth rates investigated (i.e. $10^{-8.0}$ mol m^{-2} s^{-1} $\leq R_{p(calcite)} \leq 10^{-7.3}$ mol m^{-2} s^{-1}). In contrast, in the case of aragonite mineral growth rate significantly affects the isotopic composition of the precipitated solid. The $\Delta^{137/134}Ba_{aragonite\text{-}fluid}$ shows positive values up to + 0.27±0.06‰ at aragonite growth rates ≤ $10^{-8.0}$ mol m^{-2} s^{-1} but negative values when growth rates are faster than this threshold value. This behaviour can be well explained using the surface reaction kinetic model derived from Transition State theory and already used by DePaolo (2011) and Druhan et al. (2013) to describe Ca isotopes fractionation during calcite precipitation. Additionally, this model predicts that $\Delta^{137/134}Ba_{aragonite\text{-}fluid}$ can take values as low as -2.0‰. The equilibrium experimental and theoretical $\Delta^{137/134}Ba_{aragonite\text{-}fluid}$ values determined in this study (+0.27±0.06 and +0.34 ‰, respectively) are in excellent agreement whereas the lack of Ba isotope fractionation between calcite and the fluid contrasts with the positive theoretical value ($\Delta^{137/134}Ba_{calcite\text{-}fluid}$ = +0.17‰). This likely suggests that the coordination reduction required for the incorporation in the lattice of Ba adsorbed at calcite growing sites proceeds without isotope fractionation.

The variation in the isotopic composition of the precipitated aragonite as a function of growth rate has a potential to be used as a proxy tool for estimation of growth rate or, in the case of speleothems where growth rate can be established with other techniques, the chemical and isotopic composition of Ba in the solid phase can be used to estimate the composition of the forming fluids. Likely the same can be said for coralline aragonites that are generally grown at higher rates, however other parameters such as speciation and vital effects have here to be considered.

Acknowledgments

For their assistance with XRD and BET analyses we are thankful to Katja E. Goetschl and Alain Castillo, respectively. DFT calculations were performed using HPC resources from CALMIP (grant 2019-P1037). This work has benefitted from the insightful comments of two anonymous reviewers and those by the AE Chen Zhu. The study has been supported by DFG Forschergruppe 1644 (DFG reference IM44/10-1), the French national programme LEFE/INSU and the European Research Council under the European Union’s Horizon 2020 research and innovation program (grant agreement 646894).

References

Balan E., Blanchard M., Pinilla C. and Lazzeri M. (2014) First principles modeling of sulfate incorporation and $^{34}S/^{32}S$ isotopic fractionation in different calcium carbonates. Chem. Geol. 374–375, 84–91.

Balan, E., Noireaux, J., Mavromatis, V., Saldi, G.D., Montouillout, V., Blanchard, M., Pietrucci, F., Gervais, C., Rustad, J.R., Schott, J., Gaillardet, J., 2018. Theoretical isotopic fractionation between structural boron in carbonates and aqueous boric acid and borate ion. Geochim. Cosmochim. Acta 222, 117-129.

Balan E., Pietrucci F., Gervais C., Blanchard M., Schott J. and Gaillardet J. (2016) First-principles study of boron speciation in calcite and aragonite. Geochim. Cosmochim. Acta 193, 119–131.

Bigeleisen, J., Mayer, M.G., 1947. Calculation of equilibrium constants for isotopic exchange reactions. J. Chem. Phys. 15, 261–267.

Blanchard, M., Balan, E., and Schauble, E.A., 2017. Equilibrium fractionation of non-traditional isotopes: A molecular modelling perspective. Rev. Min. Geochem. 82, 27-63.

Boehm, F., Eisenhauer, A., Tang, J., Dietzel, M., Krabbenhoeft, A., Kisakuerek, B., Horn, C., 2012. Strontium isotope fractionation of planktic foraminifera and inorganic calcite. Geochim. Cosmochim. Acta 93, 300-314.

Böttcher M. E. and Dietzel M. (2010) Metal-ion partitioning during low-temperature precipitation and dissolution of anhydrous carbonates and sulfates. In EMU notes in mineralogy, pp. 139–187.

Böttcher, M.E., Geprags, P., Neubert, N., von Allmen, K., Pretet, C., Samankassou, E., Nagler, T.F., 2012. Barium isotope fractionation during experimental formation of the double carbonate $BaMn[CO_3]_2$ at ambient temperature. Isot. Environ. Health Stud. 48, 457-463.

Böttcher, M.E., Neubert, N., von Allmen, K., Samankassou, E., Nägler, T.F., 2018a. Barium isotope fractionation during the experimental transformation of aragonite to witherite and of gypsum to barite, and the effect of ion (de)solvation. Isot. Environ. Health Stud. 54, 324 - 335.

Böttcher, M.E., Neubert, N., Escher, P., von Allmen, K., Samankassou, E., Nagler, T.F., 2018b. Multi-isotope (Ba, C, O) partitioning during experimental carbonatization of a hyper-alkaline solution. Chem Erde-Geochem. 78, 241-247.

Brunauer, S., Emmett, P.H., Teller, E., 1938. Adsorption of Gasses in Multimolecular layers. Journal of American Chemical Society 60, 309-319.

Chou, L., Garrels, R. M. and Wollast R. (1989) Comparative study of the kinetics and mechanisms of dissolution of carbonate minerals. Chem. Geol. 78, 269-282.

Chow, T.J., Goldberg, E.D., 1960. On the marine geochemistry of barium. Geochim. Cosmochim. Acta20, 192–198.

D'Angelo, P., Pavel, N.V., Roccatano, D., 1996. Multielectron excitations at the L edges of barium in aqueous solution. Phys. Rev. B 54, 12129-12138.

DePaolo, D.J., 2011. Surface kinetic model for isotopic and trace element fractionation during precipitation of calcite from aqueous solutions. Geochim. Cosmochim. Acta 75, 1039-1056.

de Villiers, J. P. R. 1971. Crystal structures of aragonite, strontianite, and witherite. American Mineralogist, 56, 758-767

Dietzel, M., Gussone, N., Eisenhauer, A., 2004. Co-precipitation of Sr^{2+} and Ba^{2+} with aragonite by membrane diffusion of CO_2 between 10 and 50 ^{o}C. Chem. Geol. 203, 139-151.

Druhan, J.L., Steefel, C.I., Williams, K.H., DePaolo, D.J., 2013. Calcium isotope fractionation in groundwater: Molecular scale processes influencing field scale behavior. Geochim. Cosmochim. Acta 119, 93-116.

Eyring, H., 1935. The activated complex in chemical reactions. J. Chem. Phys. 3, 107-115.

Finch, A. A., and N. Allison (2007), Coordination and local relaxation around Sr and Mg in calcite and aragonite, Miner. Mag., 71, 519–532.

Finch, A.A., Allison, N., Steaggles, H., Wood, C.V., Mosselmans, J.F.W., 2010. Ba XAFS in Ba-rich standard minerals and the potential for determining Ba structural state in calcium carbonate. Chem. Geol. 270, 179-185.

Füger A., Bruggman S., Frei R., Leis A., Dietzel M. and Mavromatis V. (2019b) The role of pH on Cr(VI) partitioning and isotopic fractionation during its incorporation in calcite. Geochim. Cosmochim. Acta 265, 520-532.

Füger A., Konrad F., Leis A., Dietzel M. and Mavromatis V. (2019a) Effect of growth rate and pH on lithium incorporation in calcite. Geochim. Cosmochim. Acta 248, 14–24.

Garrity, K. F.; Bennett, J. W.; Rabe, K. M.; Vanderbilt, D. Pseudopotentials for high-throughput DFT calculations. Comput. Mater. Sci. 2014, 81, 446−452.

Geyman, B. M., Ptacek, J. L., LaVigne, M., & Horner, T. J. (2019). Barium in deep-sea bamboo corals: Phase associations, barium stable isotopes, & prospects for paleoceanography. Earth Planet. Sci. Lett. 525, 115751.

Giannozzi, P. et al. (2009) Quantum ESPRESSO: a modular and open-source software project for quantum simulations of materials. J. Phys., Condens. Matter, 21, 395502.

Goetschl K. E., Purgstaller B., Dietzel M. and Mavromatis V. (2019) Effect of sulfate on magnesium incorporation in low-magnesium calcite. Geochim. Cosmochim. Acta 265, 505– 519.

Gussone N., Bohm F., Eisenhauer A., Dietzel M., Heuser A., Teichert B. M. A., Reitner J., Worheide G. and Dullo W. C. (2005) Calcium isotope fractionation in calcite and aragonite. Geochim. Cosmochim. Acta 69, 4485–4494.

Gussone N. and Dietzel M. (2016) Calcium isotope fractionation during mineral precipitation from aqueous solution. In Calcium Stable Isotopes Geochemistry (ed. J. Hoefs). Springer, Chap. III.

Gutjar, A., Dabringhaus, H., Lacmann, R. (1996) Studies of the growth and dissolution kinetics of the $CaCO_3$ polymorphs calcite and aragonite II. The influence of the divalent additives on the growth and dissolution rates. J. Crystal Growth 158, 310-315.

Hall J. M. and Chan L.-H. (2004) Ba/Ca in benthic foraminifera: thermocline and middepth circulation in the North Atlantic during the last glaciation. Paleoceanography 19, PA4018.

Hemsing, F., Hsieh, Y.T., Bridgestock, L., Spooner, P.T., Robinson, L.F., Frank, N., Henderson, G.M., 2018. Barium isotopes in cold-water corals. Earth Planet. Sci. Lett. 491, 183-192.

Hofmann, A.E., Bourg, I.C., Depaolo, D.J., 2012. Ion desolvation as a mechanism for kinetic isotope fractionation in aqueous systems. Proceedings of the National Academy of Sciences of the United States of America 109, 18689-18694.

Horner, T.J., Kinsley, C.W. and Nielsen, S.G. (2015) Barium-isotopic fractionation in seawater mediated by barite cycling and oceanic circulation. Earth Planet. Sci. Lett. 430, 511-522.

Horner, T.J., Pryer, H.V., Nielsen, S.G., Crockford, P.W., Gauglitz, J.M., Wing, B.A. and Ricketts, R.D. (2017) Pelagic barite precipitation at micromolar ambient sulfate. Nat. Commun. 8, 11.

Immenhauser, A., Buhl, D., Richter, D., Niedermayr, A., Riechelmann, D., Dietzel, M., Schulte, U., 2010. Magnesium-isotope fractionation during low-Mg calcite precipitation in a limestone cave - Field study and experiments. Geochim. Cosmochim. Acta 74, 4346-4364.

Jeandel, C., Dupré, B., Lebaron, G., Monnin, C., Minster, J.-F., 1996. Longitudinal distributions of dissolved barium, silica and alkalinity in the western and southern Indian Ocean. Deep-Sea Res., A, Oceanogr. Res. Pap.43, 1–31.

Li, W., Beard, B.L., Li, C., Xu, H., Johnson, C.M., 2015. Experimental calibration of Mg isotope fractionation between dolomite and aqueous solution and its geological implications. Geochim. Cosmochim. Acta 157, 164-181.

Li, W., Chakraborty, S., Beard, B.L., Romanek, C.S., Johnson, C.M., 2012. Magnesium isotope fractionation during precipitation of inorganic calcite under laboratory conditions. Earth Planet. Sci. Lett. 333-334, 304-316.

Lincoln S. F. and Merbach A. E. (1995) Substitution reactions of solvated metal ions. In Advances in Inorganic Chemistry, vol. 42 (ed. A. G. Sykes). pp. 1–88.

Liu, Y., Li, X.H., Zeng, Z., Yu, H.M., Huang, F., Felis, T., Shen, C.C., 2019. Annually-resolved coral skeletal delta Ba-138/134 records: A new proxy for oceanic Ba cycling. Geochim. Cosmochim. Acta 247, 27-39.

Lorens, R.B., 1981. Sr, Cd, Mn and Co distribution coefficients in calcite as a function of calcite precipitation rate. Geochim. Cosmochim. Acta 45, 553-561.

Lorrain A., Gillikin D. P., Paulet Y. M., Chauvaud L., Le Mercier A., Navez J. and André L. (2005) Strong kinetic effects on Sr/ Ca ratios in the calcitic bivalve Pecten maximus. Geology 33, 965–968.

Mavromatis, V., Gautier, Q., Bosc, O., Schott, J., 2013. Kinetics of Mg partition and Mg stable isotope fractionation during its incorporation in calcite. Geochim. Cosmochim. Acta 114, 188-203.

Mavromatis, V., Goetschl, K.E., Grengg, C., Konrad, F., Purgstaller, B., Dietzel, M., 2018. Barium partitioning in calcite and aragonite as a function of growth rate. Geochim. Cosmochim. Acta 237, 65-78.

Mavromatis, V., Gonzalez, A.G., Dietzel, M., Schott, J., 2019. Zinc isotope fractionation during the inorganic precipitation of calcite - Towards a new pH proxy. Geochim. Cosmochim. Acta 244, 99-112.

Mavromatis, V., Harrison, A.L., Eisenhauer, A., Dietzel, M., 2017a. Strontium isotope fractionation during strontianite ($SrCO_3$) dissolution, precipitation and at equilibrium. Geochim. Cosmochim. Acta 218, 201-214.

Mavromatis, V., Immenhauser, A., Buhl, D., Purgstaller, B., Baldermann, A., Dietzel, M., 2017b. Effect of organic ligands on Mg partitioning and Mg isotope fractionation during low-temperature precipitation of calcite in the absence of growth rate effects. Geochim. Cosmochim. Acta 207, 139-153.

Mavromatis, V., Montouillout, V., Noireaux, J., Gaillardet, J., Schott, J., 2015. Characterization of boron incorporation and speciation in calcite and aragonite from co-precipitation experiments under controlled pH, temperature and precipitation rate. Geochim. Cosmochim. Acta 150, 299-313.

Mavromatis, V., Pearce, C.R., Shirokova, L.S., Bundeleva, I.A., Pokrovsky, O.S., Benezeth, P., Oelkers, E.H., 2012. Magnesium isotope fractionation during hydrous magnesium carbonate precipitation with and without cyanobacteria. Geochim. Cosmochim. Acta 76, 161-174.

Mavromatis, V., Purgstaller, B., Dietzel, M., Buhl, D., Immenhauser, A., Schott, J., 2017c. Impact of amorphous precursor phases on magnesium isotope signatures of Mg-calcite. Earth Planet. Sci. Lett. 464, 227-236.

Mavromatis, V., van Zuilen, K., Purgstaller, B., Baldermann, A., Nägler, T.F., Dietzel, M., 2016. Barium isotope fractionation during witherite ($BaCO_3$) dissolution, precipitation and at equilibrium. Geochim. Cosmochim. Acta 190, 72-84.

Monkhorst, H. J.; Pack, J. D. Special points for Brillouin-zone integrations. Phys. Rev. B, 1976, 13, 5188-5192.

Monnin, C., Galinier, C., 1988. The solubility of celestite and barite in electrolyte-solutions and natural-waters at 25°C a thermodynamic study. Chem. Geol. 71, 283-296.

Montaggioni L. F., Le Comec F., Corrège T. and Cabioch G. (2006) Coral barium/calcium record of mid-Holocene upwelling activity in New Caledonia, South-West Pacific. Palaeogeogr. Palaeoclimatol. Palaeoecol. 237, 436–455.

Mucci, A., Morse, J.W., 1983. The incorporation of Mg^{2+} and Sr^{2+} into calcite overgrowths; influences of growth rate and solution composition. Geochim. Cosmochim. Acta 47, 217-233.

Noireaux, J., Mavromatis, V., Gaillardet, J., Schott, J., Montouillout, V., Louvat, P., Rollion-Bard, C., Neuville, D.R., 2015. Crystallographic control on the boron isotope paleo-pH proxy. Earth Planet. Sci. Lett. 430, 398-407.

Oelkers, E.H., Berninger, U.N., Perez-Fernandez, A., Chmeleff, J., Mavromatis, V., 2018. The temporal evolution of magnesium isotope fractionation during hydromagnesite dissolution, precipitation, and at equilibrium. Geochim. Cosmochim. Acta 226, 36-49.

Oelkers, E.H., von Strandmann, P., Mavromatis, V., 2019. The rapid resetting of the Ca isotopic signatures of calcite at ambient temperature during its congruent dissolution, precipitation, and at equilibrium. Chem. Geol. 512, 1-10.

Parkhurst D. L. and Appelo C. A. J. (1999) User's guide to PHREEQC (Version 2)—a computer program for speciation, bath-reaction, one-dimensional transport, and inverse geochemical calculations. Water-Resources Investigations Report 99–4259. USGS, Denver CO, USA.

Pearce, C.R., Saldi, G.D., Schott, J., Oelkers, E.H., 2012. Isotopic fractionation during congruent dissolution, precipitation and at equilibrium: Evidence from Mg isotopes. Geochim. Cosmochim. Acta 92, 170-183.

Perdew, J. P.; Burke, K.; Ernzerhof, M. Generalized gradient approximation made simple, Phys. Rev. Lett., 1996, 77, 3865-3868.

Persson, I., Sandstrom, M., Yokoyama, H., Chaudhry, M., 1995. Structure of the solvated strontium and barium ions in aqueous, dimethyl-sulfoxide and pyridine solution, and crystal-structure of strontium and barium hydroxide octahydrate. Z. Naturfors. Sect. A-J. Phys. Sci. 50, 21-37.

Pingitore, Jr., N. E. and Eastman M. P. (1984) The experimental partitioning of Ba^{2+} into calcite. Chem. Geol. 45, 113–120.

Pokrovsky, O.S., Schott, J., 2002. Surface Chemistry and Dissolution Kinetics of Divalent Metal Carbonates. Environ. Sci. Technol. 36, 426-432.

Pokrovsky, O.S., Schott, J., Mielczarski, J.A., 2000. Surface speciation of dolomite and calcite in aqueous solutions. In *Encyclopedia of Surface and Colloid Science*, Marcel Dekker, New York, pp 5081-5095.

Pinilla, C., Blanchard, M., Balan, E., Natarajan, S.K., Vuilleumier, R., Mauri, F., 2015. Equilibrium magnesium isotope fractionation between aqueous Mg^{2+} and carbonate minerals: Insights from path integral molecular dynamics. Geochim. Cosmochim. Acta 163, 126-139.

Pretet, C., van Zuilen, K., Nägler, T.F., Reynaud, S., Böttcher, M.E., Samankassou, E., 2015. Constraints on barium isotope fractionation during aragonite precipitation by corals. The Depositional Record 1, 118-129.

Reeder, R.J., Lamble, G.M., Northrup, P.A., 1999. XAFS study of the coordination and local relaxation around Co^{2+}, Zn^{2+}, Pb^{2+}, and Ba^{2+} trace elements. Am. Miner. 84, 1049-1060.

Saldi, G.D., Noireaux, J., Louvat, P., Faure, L., Balan, E., Schott, J., Gaillardet, J., 2018. Boron isotopic fractionation during adsorption by calcite – Implication for the seawater pH proxy. Geochim. Cosmochim. Acta 240, 255-273.

Schauble, E.A., 2004. Applying stable isotope fractionation theory to new systems. Rev. Min. Geochem. 55, 65-111.

Schott, J., Mavromatis, V., Fujii, T., Pearce, C.R., Oelkers, E.H., 2016. The control of carbonate mineral Mg isotope composition by aqueous speciation: Theoretical and experimental modeling. Chem. Geol. 445, 120-134.

Sen, S., Stebbins, J.F., Hemming, N.G., Ghosh, B., 1994. Coordination Environments of B-Impurities in Calcite and Aragonite Polymorphs - a B-11 Mas Nmr-Study. Am. Miner. 79, 819-825.

Shen G. T. and Boyle E. A., 1988. Determination of lead, cadmium and other trace-metals in annually-banded corals. Chem. Geol. 67, 47–62.

Shirokova, L.S., Mavromatis, V., Bundeleva, I.A., Pokrovsky, O.S., Benezeth, P., Gerard, E., Pearce, C.R., Oelkers, E.H., 2013. Using Mg Isotopes to Trace Cyanobacterially Mediated Magnesium Carbonate Precipitation in Alkaline Lakes. Aquat. Geochem. 19, 1-24.

Speer, 1983. Crystal chemistry and phase relations of orthorhombic carbonates. Rev. Min. Geochem. 11, 145-189.

Tang, J., Dietzel, M., Boehm, F., Koehler, S.J., Eisenhauer, A., 2008a. Sr^{2+}/Ca^{2+} and $^{44}Ca/^{40}Ca$ fractionation during inorganic calcite formation: II. Ca isotopes. Geochim. Cosmochim. Acta 72, 3733-3745.

Tang, J., Koehler, S.J., Dietzel, M., 2008b. Sr^{2+}/Ca^{2+} and $^{44}Ca/^{40}Ca$ fractionation during inorganic calcite formation: I. Sr incorporation. Geochim. Cosmochim. Acta 72, 3718-3732.

Tang, J.W., Niedermayr, A., Kohler, S.J., Bohm, F., Kisakurek, B., Eisenhauer, A., Dietzel, M., 2012. Sr^{2+}/Ca^{2+} and $^{44}Ca/^{40}Ca$ fractionation during inorganic calcite formation: III. Impact of salinity/ionic strength. Geochim. Cosmochim. Acta 77, 432-443.

Teng, F.-Z., 2017. Magnesium Isotope Geochemistry. Rev. Min. Geochem. 82, 219-287.

Tesoriero, A.J., Pankow, J.F., 1996. Solid solution partitioning of Sr^{2+}, Ba^{2+}, and Cd^{2+} to calcite. Geochim. Cosmochim. Acta 60, 1053-1063.

van Zuilen, K., Nagler, T.F., Bullen, T.D., 2016. Barium Isotopic Compositions of Geological Reference Materials. Geostand. Geoanal. Res. 40, 543-558.

von Allmen, K., Bottcher, M.E., Samankassou, E., Nagler, T.F., 2010. Barium isotope fractionation in the global barium cycle: First evidence from barium minerals and precipitation experiments. Chem. Geol. 277, 70-77.

Wolgemuth, K., Broecker, W.S., 1970. Barium in sea water. Earth Planet. Sci. Lett.8, 372–378.

Table 1: Mineralogy, growth rate, pH, partition coefficient, saturation state of the fluid with respect to forming $CaCO_3$ mineral, isotopic composition of the solid phase and selected fluids and Ba isotope fractionation between carbonate solids and fluid in the experiments performed in this study. All the $\delta^{137/134}$Ba values express the average of duplicate analyses.

Experimental run	**Mineral phase**	**Log R_p (mol/m^2/s)**	**pH**	**LogD_{Ba}**	**Ω_{CaCO3}**	**$\delta^{137/134}$Ba**			**2 sd ***	**$\Delta^{137/134}Ba_{solid-fluid}$**	**2 sd propagated**
						repl 1	**repl 2**	**average**			
Solids											
CaBa4	calcite	-7.9	6.16	-2.24	1	0.108	0.085	0.096	0.032	0.012	0.055
CaBa5	calcite	-7.7	6.15	-2.16	1.3	0.120	0.081	0.100	0.055	0.016	0.067
CaBa7	calcite	-7.8	6.18	-2.22	1.2	0.105	0.081	0.093	0.035	0.008	0.055
CaBa8	calcite	-8	6.2	-2.32	1.2	0.070	0.105	0.087	0.050	0.003	0.063
CaBa12	calcite	-7.4	6.16	-2.19	1.1	0.046	0.073	0.060	0.038	-0.025	0.055
CaBa14	calcite	-7.3	6.18	-2.05	1.2	0.052	0.056	0.054	0.006	-0.03	0.055
CaBa25	aragonite	-9	6.23	-0.66	1.1	0.322	0.353	0.338	0.043	0.253	0.058
CaBa26	aragonite	-8.6	6.25	-0.4	1.2	0.162	0.180	0.171	0.025	0.087	0.055
CaBa27	aragonite	-8.1	6.31	-0.24	1.5	0.101	0.125	0.127	0.073	0.042	0.083
CaBa28	aragonite	-7.9	6.22	-0.17	1.6	0.053	0.053	0.053	0.001	-0.032	0.055
CaBa29	aragonite	-8.4	6.31	-0.41	1.4	0.200	0.184	0.192	0.023	0.108	0.055
CaBa30	aragonite	-8	6.27	-0.18	1.7	0.048	0.026	0.037	0.032	-0.048	0.055
CaBa31	aragonite	-8.7	6.26	-0.57	1.1	0.321	0.356	0.339	0.049	0.254	0.063
CaBa36	aragonite	-8.2	6.35	-0.4	1.5	0.068	0.073	0.070	0.007	-0.014	0.055
CaBa37	aragonite	-7.8	6.24	-0.11	2	0.044	0.041	0.043	0.005	-0.042	0.055
CaBa38	aragonite (37.2 wt.%)	-7.7	6.2	-0.57	1.6	0.048	0.017	0.032	0.044	-0.052	0.059
CaBa39	aragonite (26.5 wt.%)	-7.6	6.21	-0.71	2	0.031	-0.005	0.013	0.051	-0.071	0.064
CaBa40	aragonite (15.4 wt.%)	-7.6	6.13	-0.83	1.6	0.013	-0.035	-0.011	0.068	-0.095	0.078

Fluids				
$BaCl_2$-stock	0.085	0.084	0.085	0.001
CaBa5-12	0.058	0.071	0.064	0.018
CaBa8-12	0.087	0.110	0.099	0.032
CaBa14-7	0.085	0.041	0.063	0.063
CaBa25-9	0.071	0.077	0.074	0.008
CaBa29-1	0.112	0.062	0.087	0.071
CaBa29-5	0.040	0.053	0.047	0.018
CaBa29-9	0.066	0.057	0.062	0.013

* If the 2sd is smaller than ±0.039 ‰, the pooled 2 standard deviation of the sample set (±0.039 ‰) is used.

Table 2: Polynomial fits of β-factor for the four phases ($10^3\ln\beta = b.10^6/T^2$ with T in K) and α fractionation factor between each mineral and Ba-hydrate ($10^3\ln\alpha = a.10^6/T^2$ with T in K)

Coefficients	Aragonite	Calcite	Witherite	Ba-hydrate
b for β-factor	0.0917	0.0767	0.0614	0.0615
a for α-factor	0.0303	0.0152	-0.0007	/

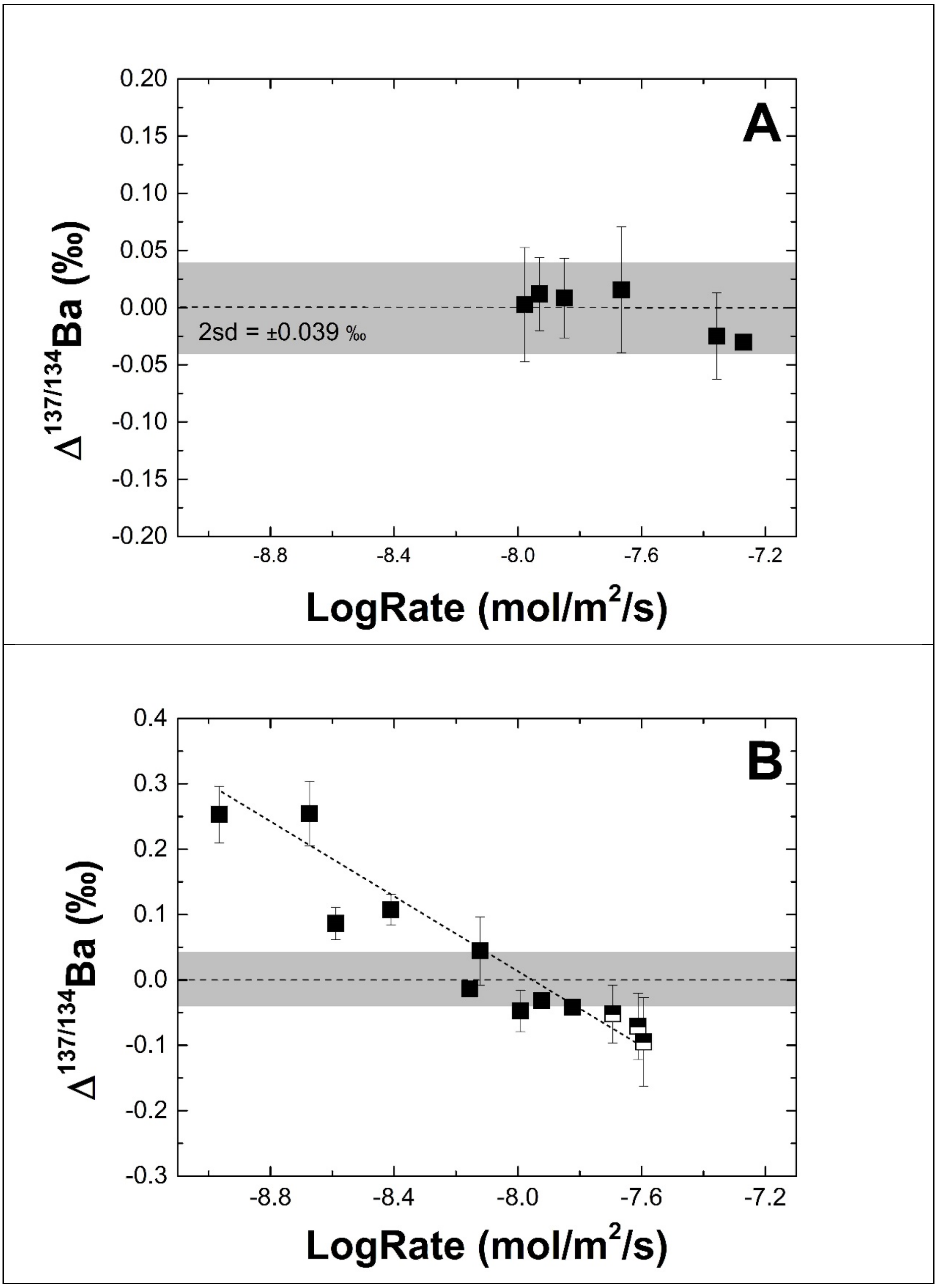

Figure 1: Ba isotope fractionation between calcite (A), aragonite (B) and fluid as a function of growth rate. Black and white symbols correspond to samples CaB38, CaB39 and CaB40, containing both calcite and aragonite overgrowths.

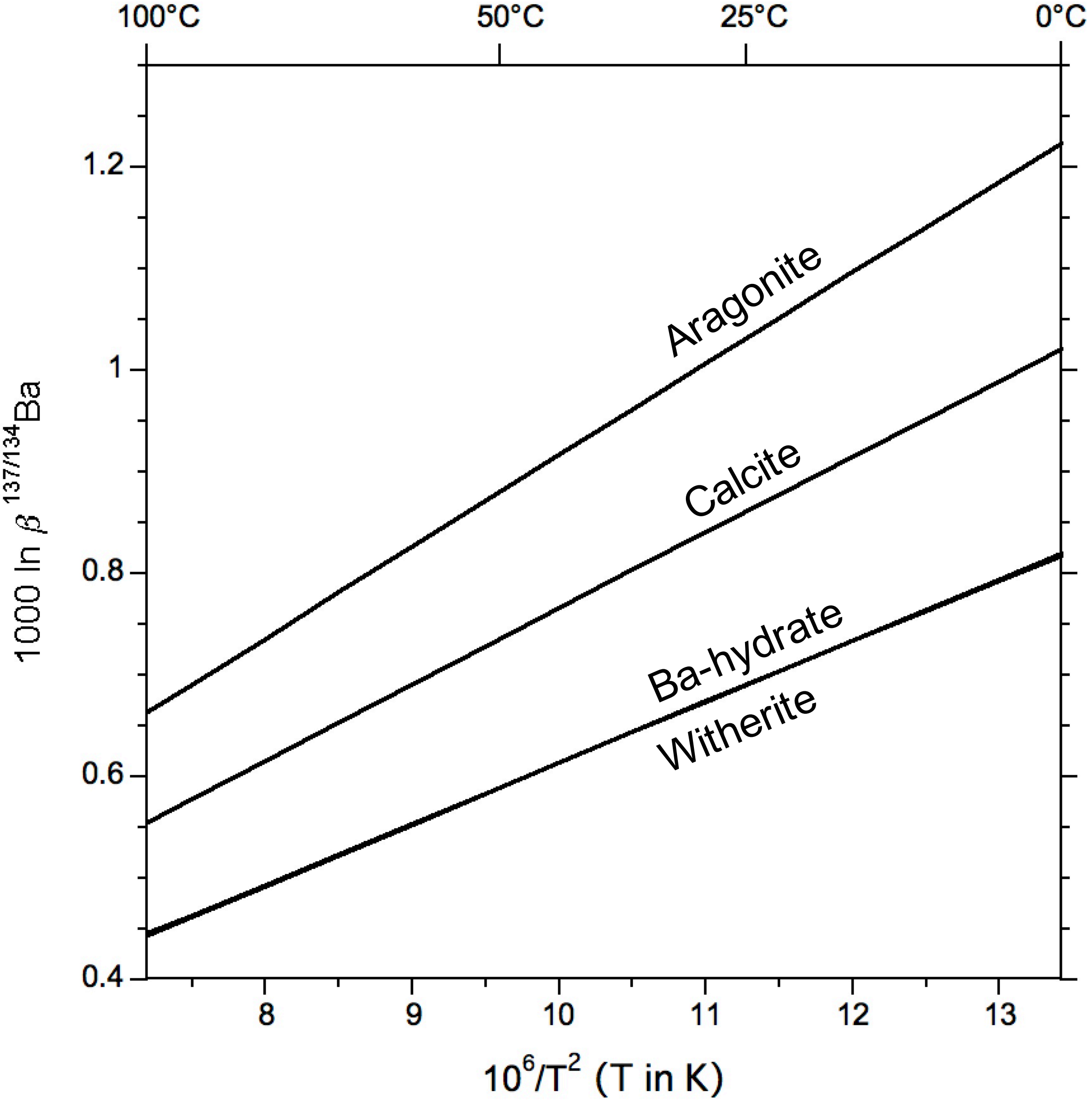

Figure 2: Theoretical temperature dependence of Ba isotope *β*-factor for aragonite, calcite, witherite and barium hydrate.

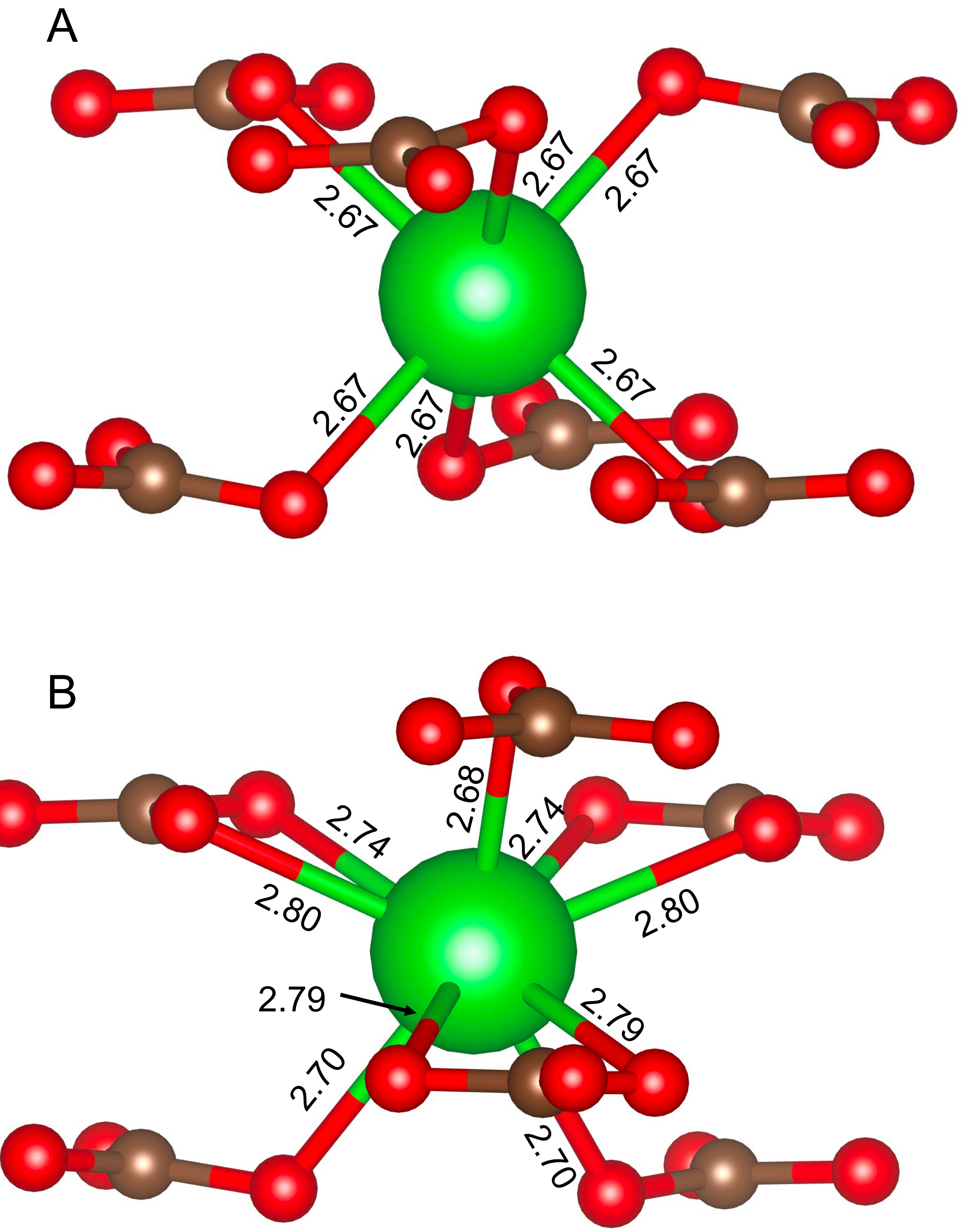

Figure 3: Local structure around Ba atom in calcite (A) and aragonite (B), from first-principles calculations. Numbers correspond to relaxed Ba-O bond lengths (in Å). Ba, O and C atoms are represented in green, red and brown, respectively.

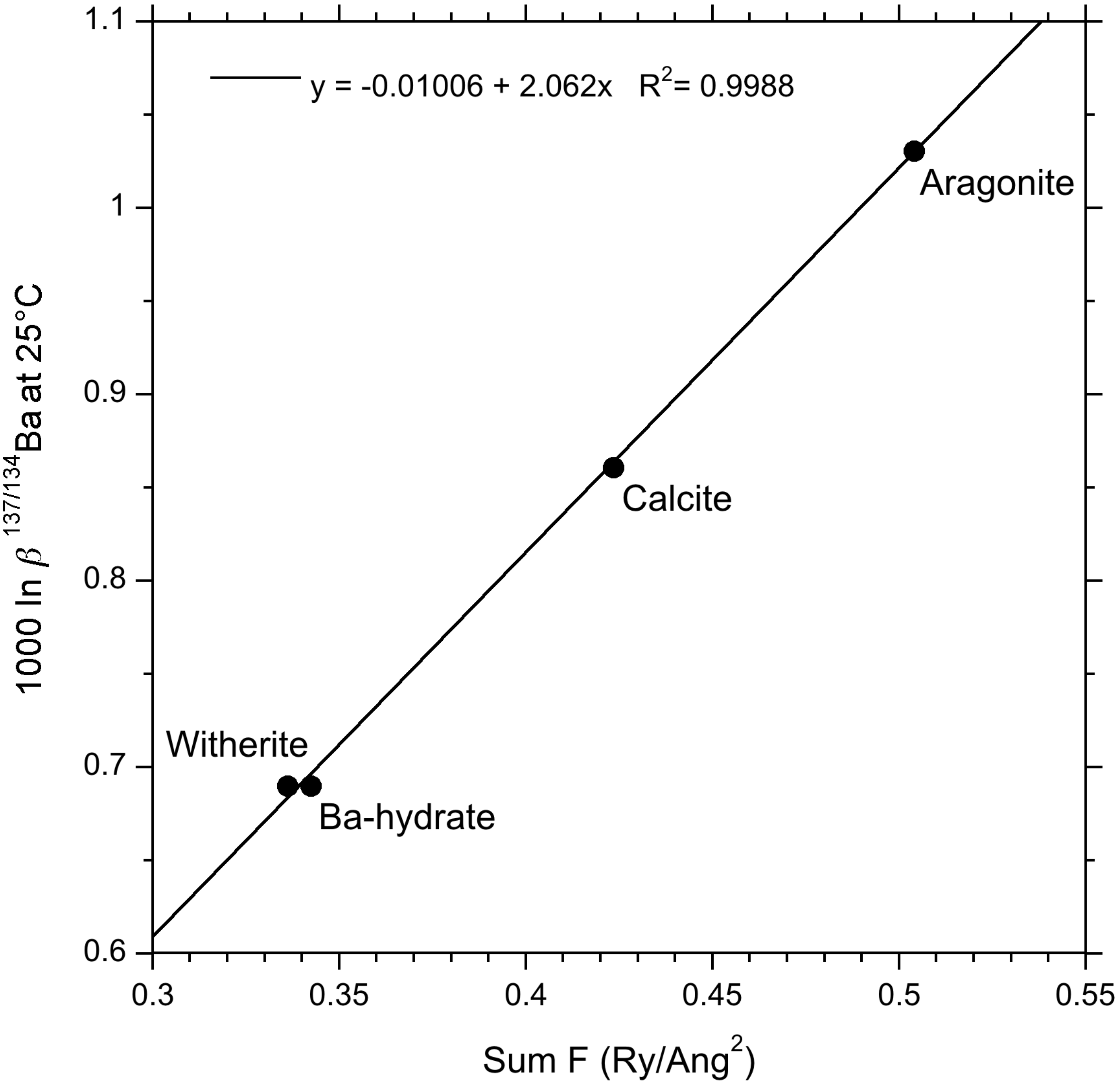

Figure 4: Theoretical Ba isotope *β*-factor at 25°C as a function of the Ba interatomic force constant.

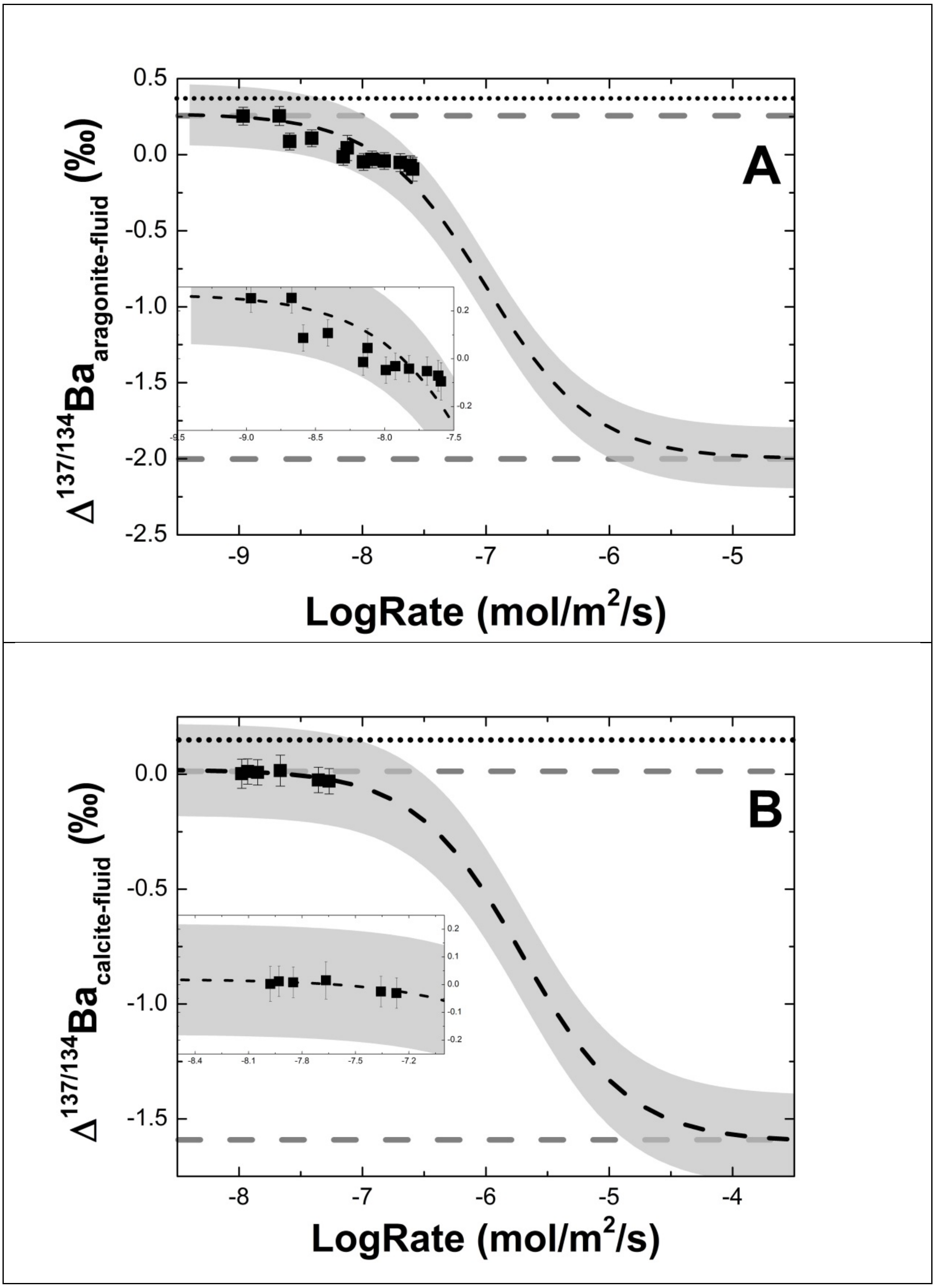

Figure 5: Best-fit line of the TST model to the experimental data for A) aragonite and B) calcite. The grey dashed lines denote the equilibrium and the maximum kinetic isotope fractionation that can be theoretical observed based on the model. The dotted line illustrates the equilibrium isotope fractionation predicted by first-principles simulations. The uncertainty of the best-fit line is ±0.2 ‰. This uncertainty has been approximated as the square root of the sum of the squares of the analytical uncertainty for the α_{eq} (i.e. ±0.06‰) and α_f (i.e ±0.2‰).

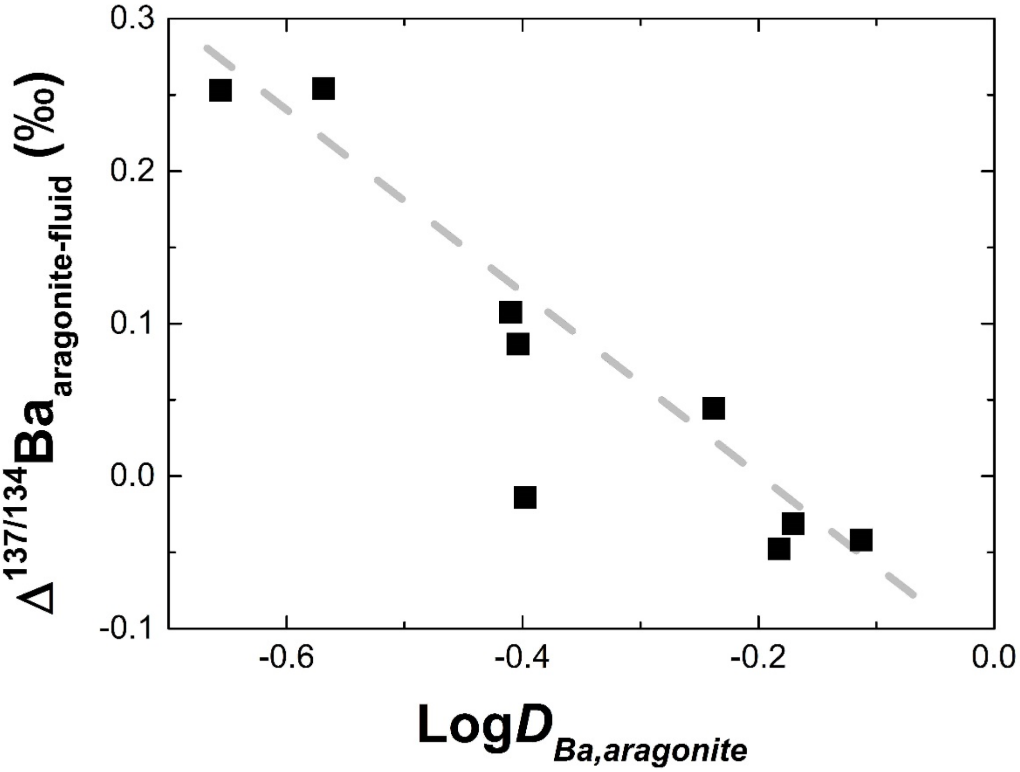

Figure 6: Barium partition coefficient of synthetic aragonite samples plotted as a function of Ba isotope fractionation between solid and fluid. The linear trend represents Eq. (19).